

Investigation of melt pool dynamics and solidification microstructures of laser melted Ti-6Al-4V powder using X-ray synchrotron imaging

Nicholas Derimow^{a,*}, Madelyn Madrigal Camacho^b, Orion L. Kafka^a, Jake T. Benzing^a, Edward J. Garboczi^a, Samuel J. Clark^c, Kamel Fezzaa^c, Suveen Mathaudhu^b, Nik Hrabe^a

^a Applied Chemicals and Materials Division, 325 Broadway, Boulder, CO 80305, USA

^b Department of Metallurgy and Materials Engineering, Golden, CO 80401, USA

^c X-ray Science Division, Advanced Photon Source, Lemont, IL 60439, USA

ARTICLE INFO

Keywords:

Additive Manufacturing
Ti-6Al-4V
X-ray synchrotron imaging
Solidification microstructure
Powder Size Distribution

ABSTRACT

Titanium alloy (Ti-6Al-4V) is widely used in additive manufacturing (AM) industry. However, as laser powder-bed fusion (PBF-L) additive manufacturing (AM) advances towards reliable production of titanium parts, a thorough understanding of the process-structure-properties (PSP) relationships remain to be fully understood. A study of the laser melting was paired with high-speed X-ray synchrotron imaging at the 32-ID beamline of the Advanced Photon Source at Argonne National Laboratory. Simultaneous melting and imaging was carried out on a Ti-6Al-4V powder layer held in a custom device designed to mimic single-track scans of the PBF-L process at different laser power levels, powder size distributions, and cover gas environments (Ar and He) on top of AM Ti-6Al-4V base metal. It was found that the thickness of the powder layer significantly affected the melt behavior: too much powder led to the formation of molten droplets that wetted the surface of the titanium, yet did not contribute to a uniform melting profile. Residual gas pores in the atomized powder were also observed to contribute to the pores observed in the melt pool, with the porosity of the powder (defined as volume of pores divided by total material volume) constant with powder size distribution (i.e., larger particles contained more entrapped gas, which increased final part porosity). When varying Ar or He through the same gas flow meter settings and nozzle, the difference in flow rates likely contributed more to the resultant porosity of the solidified material than did the thermal conductivity of the gasses, with He being the greater contributor to porosity. The microstructure of the heat affected zone contained α' , α , and an increased β phase fraction relative to the base material. The crystallographic texture of the melt pool region adopted that of the base metal.

1. Introduction

Metal-based additive manufacturing (AM) [1], particularly laser powder-bed fusion (PBF-L) [2] and laser-based directed energy deposition (DED-LB) [3] methods use a laser energy source to successively add material tracks and layers to achieve AM of a component. Whereas laser-based DED-LB processes deposit the powder with the energy source simultaneously, PBF-L requires a uniform powder layer to be deposited over the build area (powder-bed) prior to melting. Metal-based AM provides a unique opportunity to design components with complex geometries, which has led to a burgeoning industry that continues to grow both scientifically and technologically. However, the development of metal-based AM also comes with a unique set of challenges. That is, bulk pieces of metal are now comprised of thousands of microscopic melting events, which has led to the

observation of micro/macroscale porosity [4] and residual stresses imparted into the material [5]. Due to the rapid solidification that is inherent to both PBF-L and DED-LB (as well as other AM techniques), non-equilibrium/metastable microstructures tend to form, which require additional post-processing heat treatments to remove. Through investigation into the processing-structure-properties-performance (PSPP) relationships in AM materials, techniques such as X-ray synchrotron imaging have been leveraged to observe melting phenomena and phase evolution in situ [6–9,10]. Recent reviews [11,12] catalog the current state-of-the-art of X-ray synchrotron imaging as it pertains to studying AM materials.

There is a lot of interest in the AM of titanium materials [13,14] due to their high strength-to-weight ratio, good corrosion resistance, and biocompatibility. This combination of properties yields significant utility in the biomedical [15] and aerospace industries [16]. Therefore

* Corresponding author.

E-mail address: nicholas.derimow@nist.gov (N. Derimow).

<https://doi.org/10.1016/j.jalms.2024.100070>

Received 20 February 2024; Received in revised form 1 April 2024; Accepted 2 April 2024

Available online 10 April 2024

2949-9178/Published by Elsevier B.V. This is an open access article under the CC BY license (<http://creativecommons.org/licenses/by/4.0/>).

recent studies have probed the PSPP relationships in titanium, namely Ti-6Al-4V alloy, that utilize the aforementioned X-ray imaging techniques to study particle/powder movement [17], liquid-vapor interfaces [18], keyhole instabilities [19,20], and the effect of varying energy densities [21]. Recent work by the present authors [22] investigated the microstructure, mechanical properties, and phase transformations in the Ti-6Al-4V alloy (NIST SRM 645b [23]) that was used by Simonds et al. [21] during their study of laser energy density effects on melt pool behavior on bare-plate laser scans. From the modeled thermal history in Ref. [22], it was found that the heat affected zone (HAZ) in the wrought Ti-6Al-4V alloy surpassed the β -transus temperature in Ti-6Al-4V ($\approx 1000^\circ\text{C}$), and therefore lead to an increase in β phase fraction along the HAZ, as well as mixed α and acicular α' within the boundaries of the previously equiaxed α phase.

The present work studies the effects of laser melting via X-ray synchrotron imaging on AM Ti-6Al-4V. The previous studies by Simonds et al. [21] and Derimow et al. [22] investigated laser solidification on a bare surface of wrought Ti-6Al-4V (equiaxed/globular α/β microstructure), whereas the present investigation conducts the laser melting of Ti-6Al-4V powders spread on an pre-made AM Ti-6Al-4V (α/β Widmanstätten microstructure) base plate. By using AM Ti-6Al-4V as a substrate material for the powder melting, we seek to interrogate the subsequent layer in the AM process by imaging the melt pool behavior, powder behavior, and solidification microstructures through use of the simultaneous X-ray imaging and laser melting techniques at beamline 32-ID of the Advanced Photon Source, Argonne National Laboratory. While prior work has studied the impact of a powder layer, the effects of the particle size distribution has previously not been the focus of a targeted study, to our knowledge.

We tested two main hypotheses with these in-situ experiments: 1) changing the size of the powder particles will impact melting mechanics such as melt pool depth and heat affected zone size; and, 2) local thermal transport of two cover gases with different density would alter system thermodynamics, and the more thermally conductive cover gas would more effectively cool the part and reduce melt pool and heat affected zone size as well. In order to make the differences more readily measurable, high melting-point powder particles (either tungsten (W) or tantalum (Ta)) were added to enable melt pool flow characterization via particle tracking.

2. Methods and materials

2.1. Material characteristics

This work used spherical Grade 5 Ti-6Al-4V powder, conforming to ASTM¹ F2924-14 [24], which had originally been manufactured to the powder size distribution (PSD) of 45 μm to 106 μm as reported from the manufacturer via ASTM B214 [25]. This PSD is commonly used in electron beam powder bed fusion (PBF-EB). The D10, D50, and D90 (as per ASTM B822 [26]) for the Grade 5 powder was determined to be 51 μm , 70 μm , and 98 μm , respectively. A 75 μm sieve was then chosen to split the PSD of the powder in half, such that two new powder size ranges were obtained: 45 μm to 75 μm and 75 μm to 106 μm . Additional thermochemical information regarding this powder can be found in a recent thermogravimetric analysis (TGA) study of this same split PSD Grade 5 powder [27].

After sieving, each cut of powder (including the full range) was measured in 3D using X-ray computed tomography (XCT), closely following the techniques described in Refs. [28,29]. In short, a dilute suspension of particles in quick-set epoxy resin was vacuum-drawn into

¹ Commercial names are identified in order to specify the experimental procedure adequately. Such identification is not intended to imply recommendation or endorsement by NIST nor does it imply that they are necessarily the best available for the purpose.

Table 1

Number of particles analyzed, number-based averages for L, W, T, L/T, W/T, L/W, for all three sieve size ranges. SnS = single near-spherical, NS = non-spherical, mainly multi-particles. The numbers in parentheses for the W row is the arithmetic average of the sieve range limits.

Parameter	45 μm to 75 μm	75 μm to 106 μm	45 μm to 106 μm
L (μm)	69.8	116.0	76.5
W (μm)	59.6 (60)	95.5 (90.5)	65.0 (75.5)
T (μm)	57.1	89.7	62.0
L/T	1.21	1.28	1.21
W/T	1.04	1.06	1.05
L/W	1.16	1.20	1.15
No. of particles	22474	18279	17488
% SnS particles	77.1	68.8	75.9
% NS particles	22.9	31.2	24.1
Particle vol. (μm^3)	2.69×10^5	8.54×10^5	2.96×10^5

a 3 mm diameter by 50 mm long straw. After the resin cured, this was mounted vertically in a pin vise in the XCT machine. The XCT scans were conducted at 2 $\mu\text{m}/\text{pixel}$ (45 μm to 75 μm and 45 μm to 106 μm) and 2.8 $\mu\text{m}/\text{pixel}$ (75 μm to 106 μm) effective pixel size at the detector, which translates directly to cubic voxel edge length after being reconstructed into a 3D image. This ensures at least 20 voxels across the diameter of the smallest expected particles. Particles were segmented from epoxy and any air bubbles/pores, and the resulting images were used to compute particle shape parameters and identify interior pores within the particles. Data for about 20000 individual particles were collected for each cut. For each of these particles, the length (L), width (W), thickness (T) were computed using an analysis code developed at NIST [28,29]. The number-based average values for each parameter is listed in Table 1. Fig. 1 displays a secondary electron (SE) image and a reconstructed 3-dimensional image from the XCT of the full PSD of 45 μm to 106 μm powder, prior to sieving.

The average W for the 75 μm to 106 μm range is 95.5 μm , which is approximately 5.5% higher than the average of the sieve range limits (90.5 μm) for this PSD. The W for the smaller range of 45 μm to 75 μm is only 0.67% smaller than the arithmetic average of the sieve range. The particles are categorized as either *single near-spherical* (SnS) or *non-spherical* (NS) based on the previously described work [28]. For the 75 μm to 106 μm range, this resulted in 3 \times as much powder volume in this sieve size range compared to the other two. Many of the larger particles are non-spherical (NS), and likely *double particles*, given that the proportion of NS particles for the 75 μm to 106 μm range is larger than it is for the other two ranges. The proportion of NS particles in the full PSD range of 45 μm to 106 μm lies between the 45 μm to 75 μm and 75 μm to 106 μm ranges, since it is a mix of these two.

A PBF-EB piece of Ti-6Al-4V was used as the substrate for subsequent powder melting passes. It was constructed from the same virgin Grade 5 powder described above. This was done to maintain similarity of the material chemistry, simulating a postmortem microstructure when the powder had been melted onto an already additively manufactured surface (e.g. replicating the AM process by adding another layer).

The powder and base plate are from electron-beam powder-bed fusion. However, the energy source used in this work is a laser. Laser and electron beam cooling rates and microstructures are generally similar, although the heat source profile differs (volumetric versus areal). PBF-EB also more frequently uses a heated base plate. While the authors note that the as-built PBF-EB microstructure is typically a tempered α/β Widmanstätten while the as-built PBF-L microstructure is usually α' , there exists previous work that investigates the effects of a heated powder bed in PBF-L [30]. These differences should be considered when interpreting our results.

The chemical interstitial content for both the powder and as-built Ti-6Al-4V base metal is presented in Table 2. Oxygen and nitrogen were measured per ASTM E1409-13 [31], and hydrogen per ASTM E1447-09 [32], all by inert gas fusion. Carbon was measured by the combustion

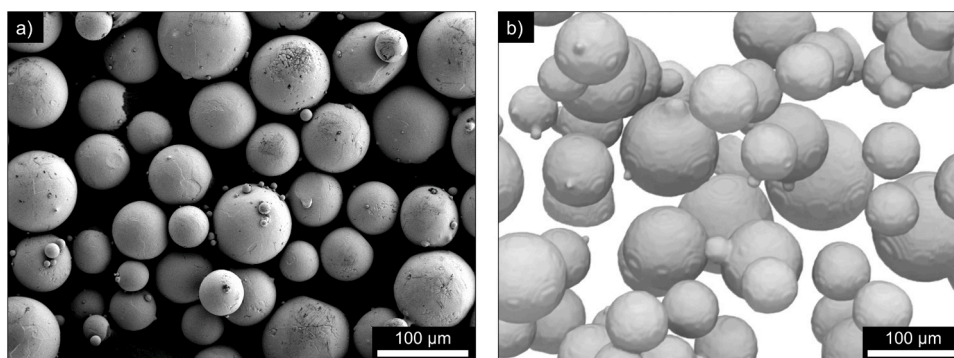


Figure 1. a) Secondary electron image of the Grade 5 Ti-6Al-4V powder with full PSD (45 μm to 106 μm) b) XCT reconstruction of the 3-dimensional particle shapes with full PSD – note, scale bar is approximate for the 3-dimensional image.

Table 2

Interstitial composition in weight % of the virgin Grade 5 powder and PBF-EB base Ti-6Al-4V metal. ASTM standard specification maximum limits for PBF Ti-6Al-4V Grade 5 (ASTM F2924 [24]) are listed with the measured values.

Weight %	O	C	N	H
ASTM 2924	0.200	0.08	0.05	0.0150
Powder	0.187	0.02	0.01	0.0020
Substrate	0.220	0.02	0.01	0.0007

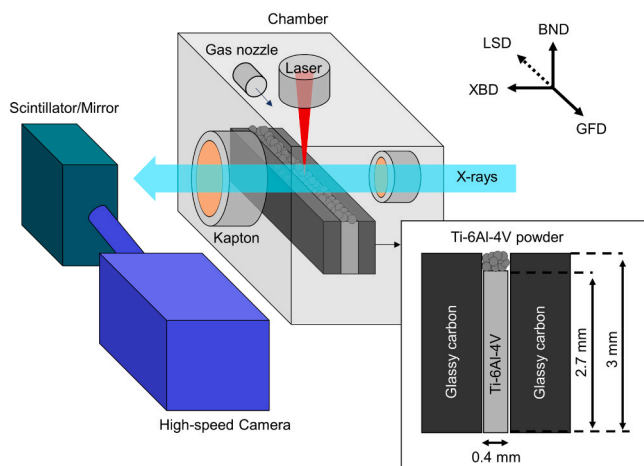


Figure 2. Diagram of the simultaneous laser melting and X-ray synchrotron imaging setup (not to scale). Coordinate system is defined as [LSD, XBD, BND] where LSD = Laser scanning direction, XBD = X-ray beam direction, and BND = (X-ray) Beam normal direction. Note, the gas flow direction (GFD) is anti-parallel to the LSD.

method per ASTM E1941–10 [33].

2.2. X-ray imaging

The techniques employed in this work utilized 32-ID-B beamline of the Advanced Photon Source (APS) at Argonne National Laboratory, as well as the same experimental setup described in Refs. [21,22], save for the integrating sphere radiometric techniques. That is, the same environmental chamber setup, laser, and mounting fixtures were used among other aspects to the experimental setup. A schematic of the this setup is provided in Fig. 2. The coordinate system used in this manuscript, pictured in the upper right hand corner of Fig. 2, consists of the laser scanning direction (LSD), X-ray beam direction (XBD), and beam normal direction (BND): [LSD, XBD, BND]. The gas flow direction (GFD) is anti-parallel to the LSD. The environmental chamber was connected to

a roughing pump which allowed for several purges/backfills (a minimum of three times) of the cover gas, either Ar or He, when specified. The viewport windows are made of kapton, such that the X-rays could travel through the chamber, be attenuated by the test piece in the center, and travel out to the detector. The X-rays are collected before, during, and after the laser melting. X-ray imaging consists of a scintillator to convert the X-rays to visible-light photons, which are collected with a conventional CCD camera to make grayscale images with an effective pixel pitch of 2 μm . A high speed camera with frame rate of 50000 frames per second (FPS) is used to capture the radiographs, which produced movies of the melting events with a temporal resolution of 20 μs between each frame. Post processing of the radiographs consisted of dividing the entire image stack by the first 50 non-moving frames for the solid melting experiments, as well as dividing by the average intensity with a Gaussian blur ($\sigma = 5$) for the powder melting image stacks. These operations provide enhanced edge contrast by emphasizing the portion of the images which differ from the initial configuration.

2.3. Laser melting

The melting was achieved through use of a continuous wave (CW) ytterbium fiber laser source with a Gaussian beam profile, wavelength of 1070 nm, and focal plane beam diameter of 41.84 μm ($D4\sigma$ value). The laser power was measured in 2019 with a NIST-traceable device that had approximately 1% uncertainty, with coverage factor $k = 2$ which corresponds to a confidence level of approximately 95.5%. Given the amount of time since then, we estimate this uncertainty could be larger. The laser was translatable in all three directions, however only the LSD and BND were translated in the experiments for melting a track of known distance in the LSD and defocusing the laser to achieve a larger beam diameter and therefore, less power density in the BND. The laser power for the melting experiments was varied at a constant defocused, conical beam diameter of 80 μm , which can be controlled manually by increasing the distance between the focal plane of the laser and melting plane. The power is discussed herein in terms of *low*, *medium*, and *high* power distributed over a 80 μm spot size, and is related as such: *Low* \approx 200 W, *Med.* \approx 260 W, and *High* \approx 320 W. The scanning speed of the laser was set to 700 mm/s for a single line of 1.4 mm, thus resulting in the laser being powered on for 2 ms for each of the single-track experiments. This track length was chosen based on previous work by Simonds et al. [21] where steady-state melting had been observed with these laser parameters.

The melting experiments utilized the PBF-EB manufactured Ti-6Al-4V alloy as the base metal, machined to 0.40 mm thickness via wire electrical discharge machining (wire EDM). The height was machined to 2.70 mm, and the length to 25.40 mm. These dimensions are therefore related to the coordinate system as such: [0.40 mm, 25.40 mm, 2.70 mm]. The base metal was then sandwiched between two glassy carbon slides, which were 3.00 mm in the BND. Therefore, this created a small

Table 3

Test matrix of varying cover gas and powder size range.

Variables	Ar	He
Solid	Ar [Ti] _{Solid} ^{Med}	He [Ti] _{Solid} ^{Med}
45 μm to 75 μm	Ar [Ti] ₄₅₋₇₅ ^{Med}	He [Ti] ₄₅₋₇₅ ^{Med}
75 μm to 106 μm	Ar [Ti] ₇₅₋₁₀₆ ^{Med}	He [Ti] ₇₅₋₁₀₆ ^{Med}
45 μm to 106 μm	Ar [Ti] ₄₅₋₁₀₆ ^{Med}	He [Ti] ₄₅₋₁₀₆ ^{Med}

Table 4

Test matrix varying tracer particle type (W or Ta) and input laser power.

Variables	Ti + 14 wt% W	Ti + 24 wt% Ta
Low (200 W)	Ar [Ti+W] ₇₅₋₁₀₆ ^{Low}	Ar [Ti+Ta] ₇₅₋₁₀₆ ^{Low}
Med (260 W)	Ar [Ti+W] ₇₅₋₁₀₆ ^{Med}	Ar [Ti+Ta] ₇₅₋₁₀₆ ^{Med}
High (320 W)	Ar [Ti+W] ₇₅₋₁₀₆ ^{High}	Ar [Ti+Ta] ₇₅₋₁₀₆ ^{High}

gap between the base metal and the glassy carbon, allowing for powder to be filled inside of the 0.30 mm tall gap in the BND. The Ti-6Al-4V powder was lightly spread on top of the carbon-titanium-carbon sandwich, filling in the 0.30 mm gap, and the plane was spread to be approximately level with the glassy carbon with a plastic scraper. The powder setup was not tapped. The melting experiments consisted of using both PSDs (45 μm to 75 μm and 75 μm to 106 μm) of the Grade 5 Ti-6Al-4V for the in situ melting experiments, as well as two cover gases: Ar and He. Melting experiments on bare (non-powder) substrates utilized 3.00 mm height versions of the solid Ti-6Al-4V for baseline comparisons of melting with the same laser settings in both gas types.

The first test matrix for the parameter set is presented in Table 3, where two PSDs and two cover gasses (Ar and He) were chosen. The flowmeter was set to 3 SLPM (standard liter per minute airflow). Thus, the Ar had a flow rate of about 2.6 SLPM whereas the He was about 6.5 SLPM, both approximated from flow rate conversion tables for air, Ar, and He. The GFD is anti-parallel to the LSD.

In order to concisely keep track of which experimental parameter is being discussed, we use the following nomenclature:

$$\text{Gastype}[\text{Element}]_{\text{Powder size range}}^{\text{Laser power (Low/Med/High)}}$$

A second test matrix (Table 4) was chosen using the Ar [Ti]₇₅₋₁₀₆^{Med} test conditions as the basis for adding high melting point element powders of tungsten (W) and tantalum (Ta) and varying the input laser power from Low to High. The mass percentage of W in the Ti+W powder was approximately 14%, whereas the mass percentage of Ta in the Ti+Ta powder was approximately 24%. These powder combinations were roughly mixed via shaking the container vials by hand, prior to manual spreading.

2.4. Particle tracking

In experiments with tracer particles, we use particle tracking to compute particles speeds, which are a proxy for flow speed of the molten metal. Particles were tracked using the Manual Tracking [34] and TrackMate [35] plugins for Fiji [36]. The two-dimensional coordinates (y, z – the LSD and BND) and their displacements were calculated in singular frame iterations using:

$$\Delta y = |y_n - y_{n-1}|, \quad \Delta z = |z_n - z_{n-1}| \quad (1)$$

$$D = \sqrt{\Delta y^2 + \Delta z^2} \quad (2)$$

where D is the displacement, subscript n indicated the current frame, and $n - 1$ indicates the previous frame. The distance was utilized to approximate particle speed by dividing D by the particle traveling time t :

$$s_{2D} = D/t \quad (3)$$

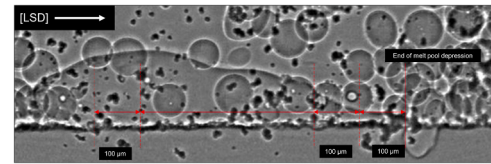


Figure 3. Example of how the distance measurements binned into 100 μm increments were taken of particles used as tracers across the melt pool.

Because consecutive frames were used, the traveling time corresponds to the time interval between the two frames (20 μs). To calculate the speed as a function of location across the melt pool, the total melt pool length was binned into 100 μm segments and the average speed within each bin computed from the distances traveled by particles within that bin, as shown schematically in Fig. 3. Note that particle speed is computed only in-plane, i.e., out of plane motion would be tracked as slowing of the particle.

2.5. Metallography

Optical microscope images of the top layers of melted powder were acquired with a stereoscopic microscope. Postmortem microstructural characterization was carried out via standard metallographic grinding and polishing techniques in the LSD-BND plane, with extreme caution so as to bisect the melt track within the sample. Since the melt track was centered in the 400 μm thick sample, after hot-mounting the entire test piece in conductive bakelite powder, grinding approximately 200 μm of material off of the puck exposed an approximate view of the longitudinal melt track of the LSD. This longitudinal view matches that observed during the X-ray imaging. Backscatter electron (BSE) images of the microstructure of the postmortem melt tracks were taken with a field emission scanning electron microscope (SEM) operated at 25 kV. Electron backscatter diffraction (EBSD) was also conducted with an EBSD step size of 0.25 μm and indexed both alpha (α) and beta (β) phases of titanium.

3. Results and discussion

3.1. Solid melting

In order to understand the effects of the processing atmosphere on the melting dynamics of the Ti-6Al-4V alloy, laser melting was conducted at Med power without any powder layer, such that the machined Ti-6Al-4V specimens were 3.00 mm in height and level with the glassy carbon slides. These specimens are labeled Ar [Ti]_{Solid}^{Med} and He [Ti]_{Solid}^{Med} and are compared against each other in Fig. 4. The radiographs in Fig. 4 display Ar on the left hand side and He on the right hand side at the same time intervals for the melting (full videos at 24 frames per second can be found in the Supplementary Information). The melting occurs from left to right, with the gas flow in the opposite direction to the laser path (anti-parallel). The laser is turned on at $t = 0.0$ ms, and radiographs are shown at $t = 0.3$ ms, $t = 1.16$ ms, $t = 1.98$ ms (just before the laser is turned off at 2.0 ms), and $t = 3.24$ ms (well after the laser has been turned off and solidification has concluded). After the initial laser exposure onto the metal, a keyhole can be seen to form in both cover gas cases at $t = 0.3$ ms (Fig. 4a–b), followed by transition mode/steady-state melting (Fig. 4c–d) with relatively similar melt pool depths at approximately 142 μm from the surface in the BND for Ar [Ti]_{Solid}^{Med} and 158 μm for He [Ti]_{Solid}^{Med} (Fig. 4e–f). For these bare-plate scans, the melt pool depth was measured as the largest vertical distance (in the BND) from the surface to the solid-liquid interface. Qualitatively, the melt pool behavior seems generally similar for both cover gases, which is consistent with work by Pauzon et al. [37].

The average solidification front velocity was calculated for both

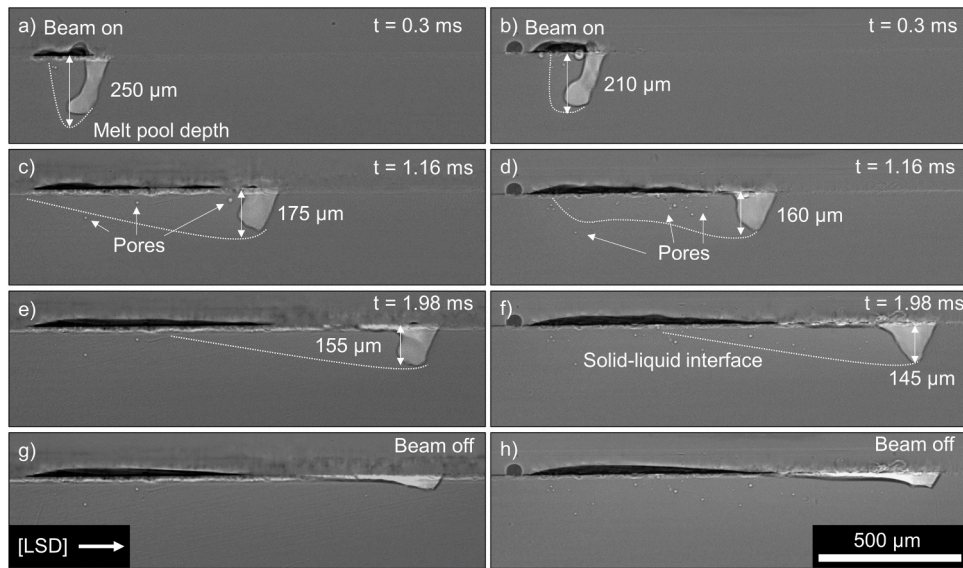


Figure 4. Radiographs of laser melting of the solid Ti-6Al-4V substrates in Ar (a,c,e,g) and He (b,d,f,h) at varying time intervals: a/b) 0.3 ms – just after the beam was turned on at Med power ($t = 0$ ms), c/d) $t = 1.16$ ms, e/f) $t = 1.98$ ms, and g/h) $t = 3.24$ ms (beam was turned off at 2.00 ms and solidification had already finished).

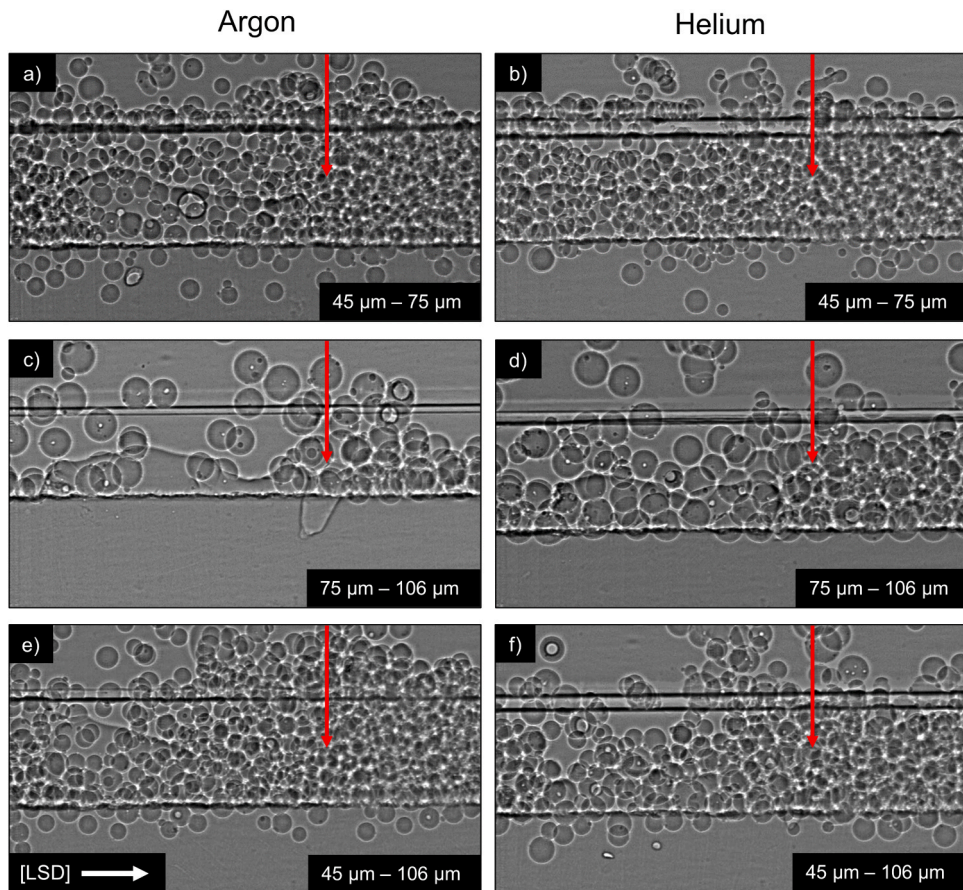


Figure 5. Radiographs of the laser melting of the power melting of the six conditions in Table 3 in Ar (a,c,e) and He (b,d,f) at 1.16 ms with Med laser power. a/b) 45 μm to 75 μm , c/d) 75 μm to 106 μm , e/f) 45 μm to 106 μm . Red downward pointing arrow indicates the laser location as it traveled from left to right. Dark horizontal lines near the top of the image are glassy carbon.

conditions by comparing individual frames of the moving solidification front after the laser was turned off (Fig. 4g–h), and was measured for both conditions to be ≈ 198 mm/s. While both test conditions contained a small number of pores, the $\text{He}[\text{Ti}]_{\text{Solid}}^{\text{Med}}$ condition had visibly more pores

than the $\text{Ar}[\text{Ti}]_{\text{Solid}}^{\text{Med}}$, as can be seen in Fig. 4d. This increase in porosity is likely due to the $\text{He}[\text{Ti}]_{\text{Solid}}^{\text{Med}}$ having almost double the volumetric flow rate of gas when compared to the $\text{Ar}[\text{Ti}]_{\text{Solid}}^{\text{Med}}$ condition given that the flow meter valve was kept constant at 3.0 SLPM of air, resulting in the two

different volumetric flow rates for Ar (approximately 2.6 SLPM) and He (approximately 6.5 SLPM). The velocity of the solidification front did not change (to within our measurement uncertainty) between the two cover gas cases. We estimate that convective heat transfer will be about a factor of 4.6 greater for the He cover gas (assuming predominantly laminar gas flow over a flat plate, ambient 300 K conditions, and all else being equal), due to the differences in flow rates and thermal properties of the two gasses [38]. However, the length/time scales employed in this work were not able to capture the direct effect of this difference on the solidification front velocity (and therefore cooling rate effects) across the single melt tracks. The increased flow of the He relative to the Ar resulted in an overall shallower melt pool depth (highlighted in Fig. 4) where the onset depth was 40 μm shallower in the He case. After the initial onset, the depth of the melt pool decreased and this difference in depth became smaller such that the steady-state depth in the He case was 15 μm shallower compared to the Ar case, and ultimately 10 μm shallower prior to powering off the laser. The overall shape of the moving solidification front in the He case also appeared to reach a brief steady-state (Fig. 4d) prior to penetrating deeper into the material, ultimately stabilizing at 145 μm (Fig. 4f). Conversely, the Ar case appeared to maintain a consistent moving solidification front until the laser was powered off.

3.2. Powder melting and Porosity

Fig. 5 shows radiographs of the six powder melting conditions in Table 3 (${}^{\text{Ar}}[\text{Ti}]_{45-75}^{\text{Med}}$, ${}^{\text{Ar}}[\text{Ti}]_{75-106}^{\text{Med}}$, ${}^{\text{Ar}}[\text{Ti}]_{45-106}^{\text{Med}}$, ${}^{\text{He}}[\text{Ti}]_{45-75}^{\text{Med}}$, ${}^{\text{He}}[\text{Ti}]_{75-106}^{\text{Med}}$, ${}^{\text{He}}[\text{Ti}]_{45-106}^{\text{Med}}$) all at a time of 1.16 ms out of 2.00 ms total laser scan time. Full videos of the melting are provided in the Supplementary Information. The 45 μm to 75 μm range for both gas flow species (Fig. 5a–b) displayed similar melting characteristics. The packing density of the powder is relatively high compared to the 75 μm to 106 μm condition (Fig. 5c–d). Note, packing density in this context refers to the number of powder particles per given volume. The radiographs for the 45 μm to 75 μm cases indicate that the powder layer was too thick for the laser to fully penetrate into the substrate, thereby resulting in droplet formation. Droplet formation was also observed in the full PSD cases for both Ar and He cover gases, as shown in Fig. 5e–f.

The ${}^{\text{Ar}}[\text{Ti}]_{75-106}^{\text{Med}}$ and ${}^{\text{He}}[\text{Ti}]_{75-106}^{\text{Med}}$ conditions are presented in Fig. 5c–d. The large powder range contributed to a more uniform melting profile for the ${}^{\text{Ar}}[\text{Ti}]_{75-106}^{\text{Med}}$ condition for the powder layer. Given that this powder layer was not as high, the melting also had a more uniform depth of penetration and uninterrupted laser pathway when compared to the droplet formation observed in Fig. 5a–b. Similar to the solid melting conditions, there appears to be more pores generated in the He condition, as well as less penetration into the bulk when compared to the Ar condition (due to the packing densities being slightly different).

The ${}^{\text{Ar}}[\text{Ti}]_{45-106}^{\text{Med}}$ and conditions behaved similarly to the ${}^{\text{Ar}}[\text{Ti}]_{45-75}^{\text{Med}}$, in that droplet formation occurred after the initial penetration into the substrate. The ${}^{\text{He}}[\text{Ti}]_{45-106}^{\text{Med}}$ condition melt behavior was similar to the ${}^{\text{He}}[\text{Ti}]_{75-106}^{\text{Med}}$ condition. Substrate penetration occurred with only a brief interruption in the path due to packing density differences. After the laser moved past the denser location, the melted structure more closely resembled the ${}^{\text{He}}[\text{Ti}]_{75-106}^{\text{Med}}$ condition than ${}^{\text{Ar}}[\text{Ti}]_{45-106}^{\text{Med}}$. Previous observations of melt pool instabilities due to droplet formation were observed by Guo et al. [39], which led to increased roughness of the solidified surface.

The results indicate that if a process is optimized for a specific PSD for a given powder layer thickness, switching to a different PSD may lead to uncontrolled melting events that could result in droplet formation and/or lack of fusion pores. A review of powder for PBF by Vock et al. [40] tabulates the PSD characteristics resulting from powder reuse for Ti-6Al-4V, where PSDs have been observed to narrow, coarsen, as well as remain unchanged through reuse in the the PBF process. While an intentionally extreme case in this particular study, the differences

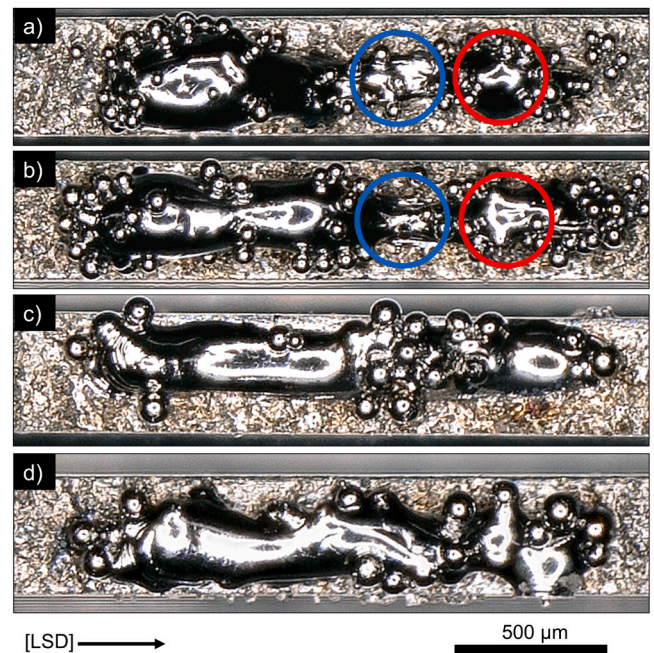


Figure 6. Optical microscope images of the melting track patterns for both Ar and He testing conditions with PSD of 45 μm to 75 μm , and 75 μm to 106 μm . a) ${}^{\text{Ar}}[\text{Ti}]_{45-75}^{\text{Med}}$, b) ${}^{\text{He}}[\text{Ti}]_{45-75}^{\text{Med}}$, c) ${}^{\text{Ar}}[\text{Ti}]_{75-106}^{\text{Med}}$, and d) ${}^{\text{He}}[\text{Ti}]_{75-106}^{\text{Med}}$.

between melting for the varying PSDs is direct evidence for suggesting the potential for PSD drift over the lifetime of a powder batch may influence the layer melting. Droplet size however, can ultimately be affected by powder packing density and dwell length of the laser as smaller molten particles could conglomerate into a larger molten particle given enough time.

Optical microscope top views of the final state of the melt tracks for the ${}^{\text{Ar}}[\text{Ti}]_{45-75}^{\text{Med}}$, ${}^{\text{Ar}}[\text{Ti}]_{75-106}^{\text{Med}}$, ${}^{\text{He}}[\text{Ti}]_{45-75}^{\text{Med}}$, and ${}^{\text{He}}[\text{Ti}]_{75-106}^{\text{Med}}$ conditions are presented in Fig. 6. The top two images (Fig. 6a–b) are of ${}^{\text{Ar}}[\text{Ti}]_{45-75}^{\text{Med}}$ and ${}^{\text{He}}[\text{Ti}]_{45-75}^{\text{Med}}$, whereas the bottom two images (Fig. 6c–d) are of ${}^{\text{Ar}}[\text{Ti}]_{75-106}^{\text{Med}}$ and ${}^{\text{He}}[\text{Ti}]_{75-106}^{\text{Med}}$. The smaller powder size range images show similar macroscopic melt patterns and droplet formation, as indicated by a lack of material towards the end of the melt track (to the right). The larger powder size range images show more uniform melt profiles with no indications of droplet formation, and are consistent with the solidified shapes observed in Fig. 5c–d. The images of the top down view for the smaller PSDs are highlighted such that the blue circles indicate where the relative powder thickness became too great due to the surrounding powder piling towards the end of the melt track. The red circles highlight where the particle droplet formed and subsequently pulled together due to the surface tension of the molten droplet.

The lighter, circular shapes inside of the powder are precursor gas pores from the atomization process, and contribute to the residual pores observed in the solidified material. The videos of the melting indicate that some of the pores that were observed in the final, solidified material may come from this precursor pores present in the atomized powder. In order to demonstrate this effect, Fig. 7 displays a single spot melting event of the powder on top of the base metal. In this case, the laser was kept static to illustrate the effect with minimized visual artifacts from the laser scanning conditions that ejected powder into the line of sight of the imaging setup. The image in Fig. 7a displays a powder particle with an entrapped precursor gas pore lying next to a forming liquid droplet on top of the base metal. As the droplet grows in size (Fig. 7b), the powder comes into contact with it, and begins to melt. Fig. 7c shows the pore now free of the powder particle, moving freely inside of the droplet. These entrapped pores are consistent with previous observations in PBF-L imaging experiments detailed in a doctoral thesis by Cunningham [41]

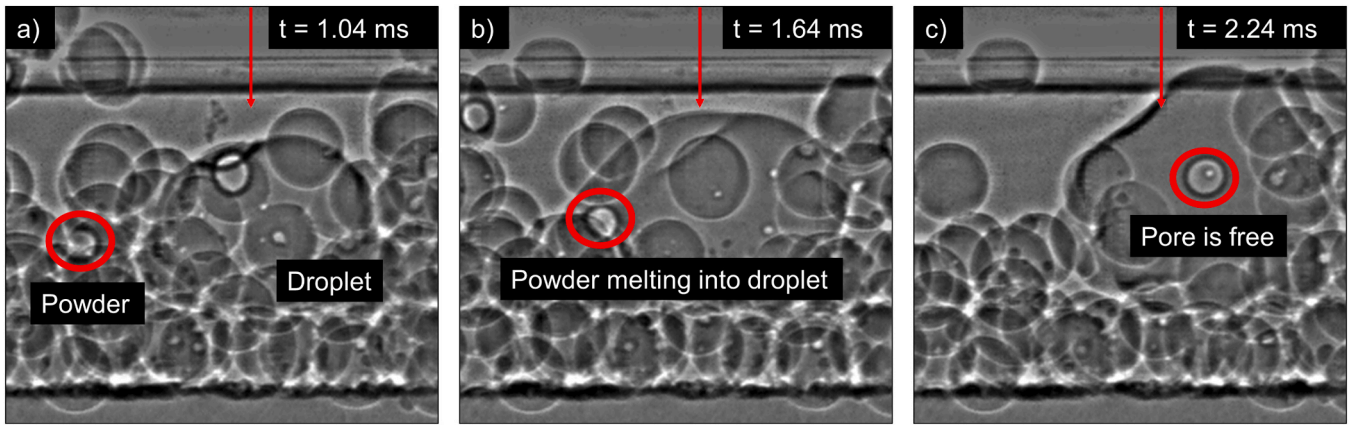


Figure 7. Radiographs of a single spot melting/droplet formation showing a) residual gas trapped inside of a powder particle, b) the powder melting into the droplet, c) the residual gas pore releasing into the melt pool. The full video of this figure can be found in the Supplementary Information.

Table 5
XCT porosity measurements of the powder particles.

Powder Class	$N_{P \neq 0}$ (%)	P_{avg} (%)
45 μm to 75 μm	4.92	0.70 ± 1.68
75 μm to 106 μm	11.70	0.87 ± 1.78
45 μm to 106 μm	8.00	0.41 ± 1.06

and in situ imaging experiments of DED AM by Wolff et al. [42]. The dynamics of bubble trajectories was modeled by Yan et al. [43], where it was determined that rising speed of the bubble is slow relative to the solid-liquid interface, which implies that precursor pores may tend to become entrapped during solidification.

The internal porosity (P) of the powders was analyzed from the XCT of the three PSDs. The percentage of porous particles ($N_{P \neq 0}$) in Table 1 show that the larger powder size range of 75 μm to 106 μm had the highest percentage of porous particles compared to the smaller size range of 45 μm to 75 μm . Given that these two PSDs were split from the 45 μm to 106 μm batch ($N_{P \neq 0} = 8.00\%$), the average of the two equates to 8.31%, which is consistent with the measurement. Within each individual PSD range, the average porosity (P_{avg}) is computed by averaging the porosities over the $N_{P \neq 0}$ particles for each PSD range, not weighted by volume. The amount of $N_{P \neq 0}$, in general, is consistent with previous observations of Ti-6Al-4V powder porosity in this PSD range for PBF-EB applications [44].

The P_{avg} for all three particle classes do not present statistical differences between each other. These values for P_{avg} , being more or less equal, implies that either the size of the pores within each particle was proportional to the particle size, or the number of pores of similar size present increased as the cube of the particle size, which seems less likely Table 5.

This phenomena may be a contributing factor to observed pores in PBF-L experiments in general, as the pore contributions from the precursor entrapped gas are not as easily investigated outside of beamline experiments. Pores, as they pertain to fatigue crack initiation were modeled via crystal plasticity by Prithivirajan and Sangid [45], where it was found that the critical (spherical) pore size was estimated to be 20 μm for PBF-L IN718 when the average grain size is 48 μm . The pore shown in Fig. 7 was approximately 25 μm , implying that precursor pores incorporated in the as-solidified part may be a pathway for the formation of fatigue-critical pores. Hot isostatic pressing (HIP) treatments have been employed to ensure fully dense AM parts in PBF-L Ti-6Al-4V [46] to close the pores leftover from either residual gas pores in the powder, gas pores directly from the PBF-L process, or gas pores entrapped from lack of fusion defects. Historically, traditional cover gasses such as Ar or He have not been observed to diffuse through metals

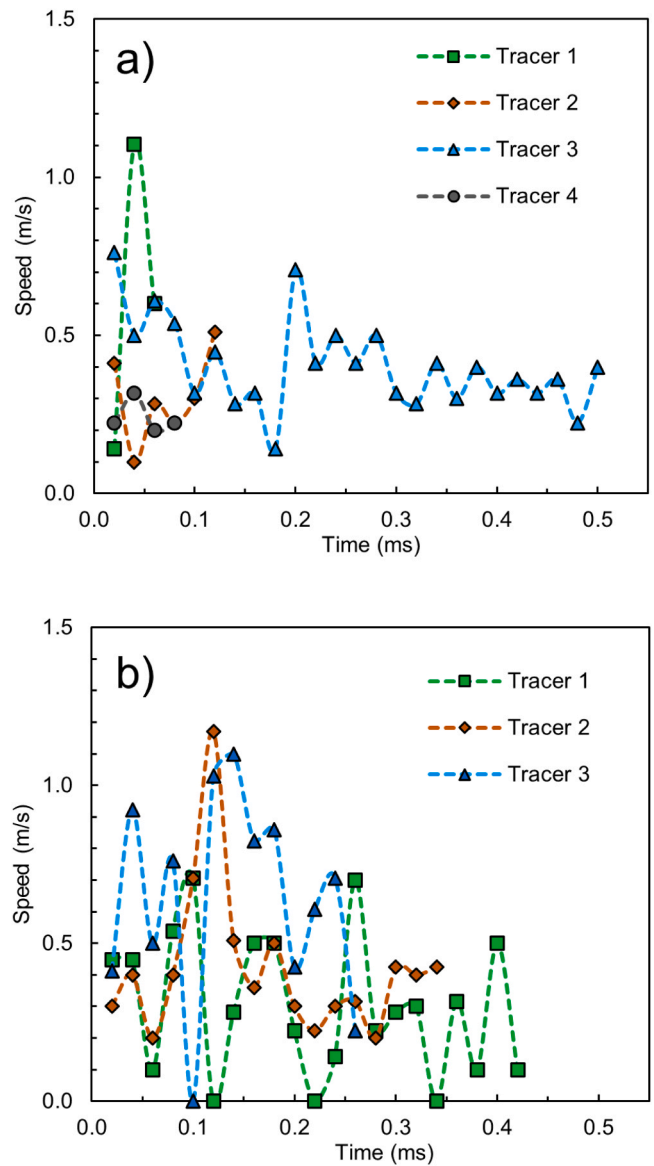


Figure 8. a) Instantaneous speed of tracers in $^{Ar}[Ti]_{45-75}^{Med}$. b) Instantaneous speed of tracers in $^{He}[Ti]_{75-106}^{Med}$.

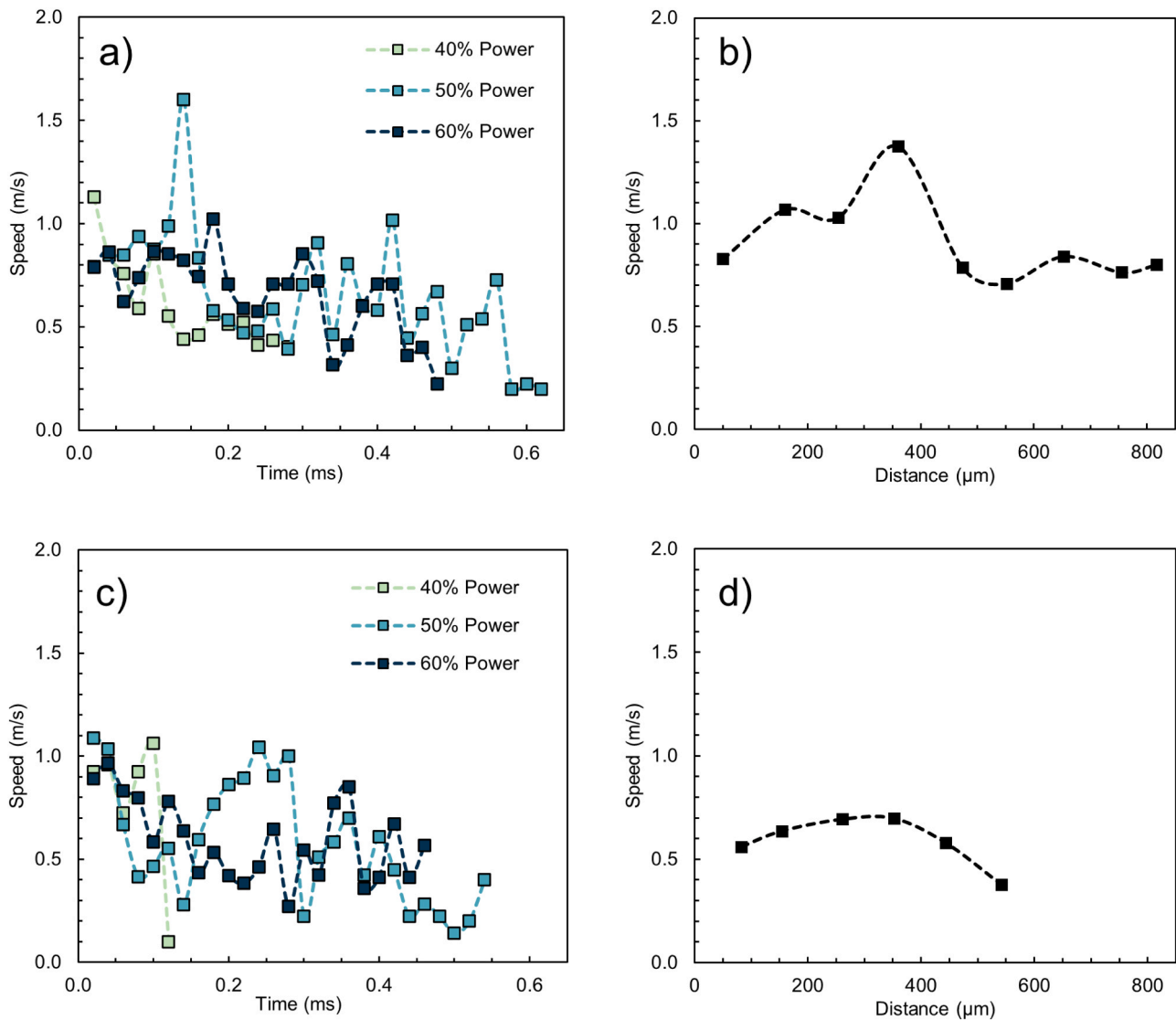


Figure 9. a) Average speed calculated within segments of 0.02 msec of sample $^{Ar}[Ti+W]_{75-106}^{Low/Med/High}$. b) Average speed of tracers within segments of $100 \mu m$ as a function of distance across the melt pool for $^{Ar}[Ti+W]_{75-106}^{Med}$. c) Average speed calculated within segments of 0.02 msec of sample $^{Ar}[Ti+Ta]_{75-106}^{Low/Med/High}$. d) Average speed of tracers within segments of $100 \mu m$ as a function of distance across the melt pool for $^{Ar}[Ti+Ta]_{75-106}^{Med}$.

[47]. Therefore, it remains an open question if the gas pores that get shrunken in size (and therefore compressed and pressurized) from HIP has the potential for deleterious effects, similar to the nanoscale pores in the form of radiation-induced He bubbles (resulting from α -decay) that are present in structural metals used in nuclear reactors [48].

3.3. Melt pool dynamics

The general shape of the melt pools correspond to conduction mode melting for samples with Med to High power. For the specimens that contain Ta and W tracer particles (Table 4), the melt flow forms a counterclockwise vortex moving backwards behind the laser beam, consistent with previous observations of flow behavior by Guo et al. [39]. No specific trends could be found for the flow direction ahead of the laser beam as the general flow speed was not quantified. For specimens $^{Ar}[Ti]_{45-75}^{Med}$, $^{Ar}[Ti]_{75-106}^{Med}$, and $^{He}[Ti]_{75-106}^{Med}$, the direction and pattern of the flow is not as clear as the points used as tracers for the powders (internal gas pores) had varying movement trends, and out-of-plane motion could not be quantified.

There was a tendency of the pores to travel at lower speeds at the

beginning of the laser melting for $^{Ar}[Ti]_{45-75}^{Med}$ (Fig. 8a) and $^{He}[Ti]_{75-106}^{Med}$ (Fig. 8b) when compared to the specimens with Ta or W added tracer particles. Specimens $^{Ar}[Ti]_{75-106}^{Med}$ and $^{He}[Ti]_{45-75}^{Med}$ did not have enough internally porous powder particles to utilize for tracing. Additionally, $^{Ar}[Ti]_{45-75}^{Med}$ and $^{He}[Ti]_{75-106}^{Med}$ samples showed more upward and downward movements across the melt pool specifically at longer distances from laser path. It was observed that due to this behavior, there is not a specific trend of the general decreasing speed as a function of time. This observation was also observed in specimens $^{Ar}[Ti+W]_{75-106}^{Low/Med/High}$ and $^{Ar}[Ti+Ta]_{75-106}^{Low/Med/High}$.

For the specimens with particle tracing, the tracers experienced a maximum speed at approximately 0.10 ms after the laser was turned on. As the melt path progressed, the rate at which the tracers decelerate was not uniform enough to quantify a mathematical trend of the flow behavior during the laser melting. The average speed of the tracers within segments of 0.02 ms for $^{Ar}[Ti+W]_{75-106}^{Low/Med/High}$ and $^{Ar}[Ti+Ta]_{75-106}^{Low/Med/High}$ were calculated and shown in Fig. 9a and c, respectively.

For all powder conditions, the speed fluctuates throughout the entire

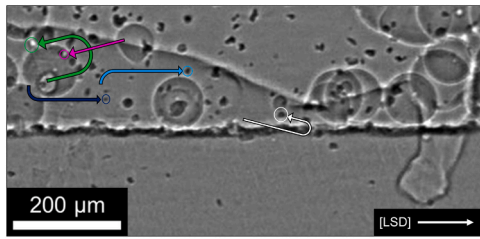


Figure 10. Instantaneous tracer trajectory in sample $^{Ar}[\text{Ti}+\text{Ta}]_{75-106}^{\text{High}}$. Green (pore) and white, counterclockwise direction moving backwards. Magenta (pore) backward and downward. Light and dark blue, forward.

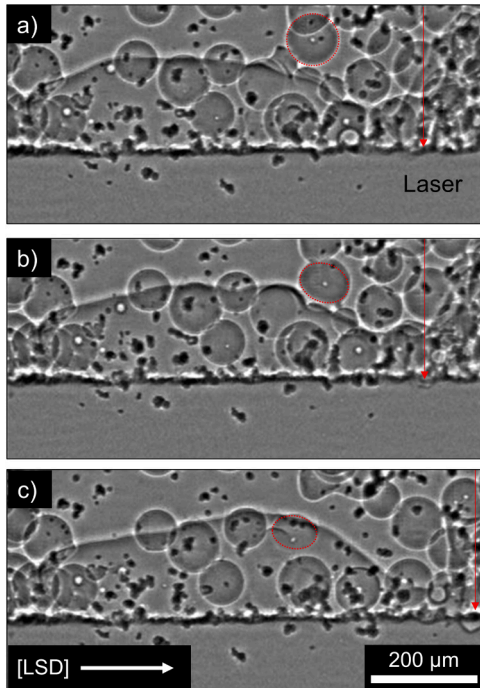


Figure 11. Particle collision with the melt pool in sample $^{Ar}[\text{Ti}+\text{W}]_{75-106}^{\text{Med}}$.

trajectory. This is caused by the changes in direction of the tracers along the melt pool. This change in direction is shown for $^{Ar}[\text{Ti}+\text{Ta}]_{75-106}^{\text{High}}$ in Fig. 10 as an example of tracer directions. To further interrogate the fluctuations in tracer speed, the average speed as a function of the distance from the melt pool depression zone was calculated in order to understand if the fluctuations are dependent of specific distances away from the laser path. Fig. 9b-d, shows that the maximum speed occurs in both $^{Ar}[\text{Ti}+\text{W}]_{75-106}^{\text{Low/Med/High}}$ (Fig. 9b) and $^{Ar}[\text{Ti}+\text{Ta}]_{75-106}^{\text{Low/Med/High}}$ (Fig. 9d) conditions at a similar distance (approximately 350 μm) from the laser beam. A decrease in speed was observed after reaching approximately 350 μm from the laser beam. For $^{Ar}[\text{Ti}+\text{Ta}]_{75-106}^{\text{Low/Med/High}}$, a slight decrease in speed was observed. However this apparent decrease in speed may be due to out-of-plane motion. For $^{Ar}[\text{Ti}+\text{W}]_{75-106}^{\text{Low/Med/High}}$, the average speed as a function of distance displays fluctuations at distances away from the laser path.

Along with out-of-plane motion, this behavior was the result of particle collisions (an example of which is shown Fig. 11 for $^{Ar}[\text{Ti}+\text{W}]_{75-106}^{\text{Med}}$) and the impact of metal droplets into the melt pool. During an impact, the droplet transfers kinetic energy into the melt pool locally altering the original flow direction. The instability of the flow direction was confirmed via postmortem SEM BSE imaging of $^{Ar}[\text{Ti}+\text{W}]_{75-106}^{\text{Med}}$ shown in Fig. 12, where the brighter particles (higher Z-contrast) are the partially dissolved W tracers. Given that W and Ti have

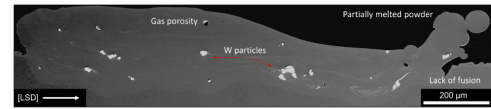


Figure 12. BSE image of $^{Ar}[\text{Ti}+\text{W}]_{75-106}^{\text{Med}}$ displaying the W particle trajectories after sectioning and polishing. Note, the image was flipped during post-processing such that the laser scanning direction can be observed from left to right.

large difference in atomic number, the W-enriched regions in the melt pool can be visually observed to follow the path of the moving W particle in a tail-like manner.

3.4. Microstructure

In order to investigate the post-solidification microstructure of the laser melting experiments, $^{Ar}[\text{Ti}]_{75-106}^{\text{Med}}$ was chosen for analysis as it had the most uniform melting behavior from the in situ imaging relative to the other specimens. The microstructure at the beginning of the melt track is presented in Fig. 13a where three distinct regions are visible due to electron channeling contrast differences when collecting back-scattered electrons. The melt pool region is shown in higher magnification in Fig. 13b, where the microstructural features are consistent with the non-equilibrium martensite (α') phase found in Ti-6Al-4V alloy as a result of rapid solidification from laser melting [49]. The heat affected zone (HAZ) is shown in Fig. 13c, where the microstructure has maintained the general morphology of the α/β Widmanstätten microstructure (Fig. 13d), however, has undergone a phase transformation in the α phase that resembles that of the α' phase, and is likely a mixture of α and α' . These observations are consistent with the microstructural observations of our previous investigation into the laser melting of wrought Ti-6Al-4V alloy [22]. The base metal (Fig. 13d) consists of α/β Widmanstätten morphology typically observed in as-built PBF-EB Ti-6Al-4V [13].

A large area BSE image of the entire melt track field of view (FOV) is shown in Fig. 14a, where in this particular case of metallographic mounting the LSD is from right to left and is detailed in the legend at the bottom of the figure. There is a small gas pore at the very beginning of the melt track, as well as partially melted/fused powder particles that adhered to the melt pool during the steady-state melting and at the end of the melt track. The pore visible inside of the end particle is precursor gas pore, confirmed from the in situ imaging video of the melting. The inverse pole figure map with underlying image quality (IQ) as grayscale of the EBSD measurement is presented in Fig. 14b, where all three regions (melt pool, HAZ, and base metal) are visible. The melt pool boundary is visible and is consistent with the melt pool boundary in the BSE image (Fig. 14a). The inverse pole figure (IPF) map shown in Fig. 14b displays the grain orientations for each of the three regions, with the texture of the melt pool adopting the base metal texture. Along the melt pool boundary in Fig. 14b, prior- β grain morphology can be observed as dark lines trending upwards towards the BND.

A prior- β reconstruction was conducted such that the parent β plane $\{110\}$ is related to the child α child plane $\{0001\}$, with corresponding parent directions of $\beta\langle 111 \rangle$ to $\alpha\langle 11\bar{2}0 \rangle$ as described in Ref. [50]. A reconstructed IPF map of the prior- β grains with underlying image quality is presented in Fig. 14c. The horizontal intercept length of the prior- β grains was measured by hand to be approximately 70 μm . However, the prior- β morphology in the melt pool region is finer, with horizontal intercept lengths measured to be approximately 7 μm to 8 μm . This factor of 10 decrease in length is likely due to the rapid solidification of the laser melted region with base metal at room temperature. Whereas, the base metal which consists of PBF-EB Ti-6Al-4V, was melted in an environment with background temperatures ranging from 600°C to 800°C. This likely led to a slower cooling rate relative to PBF-L, and

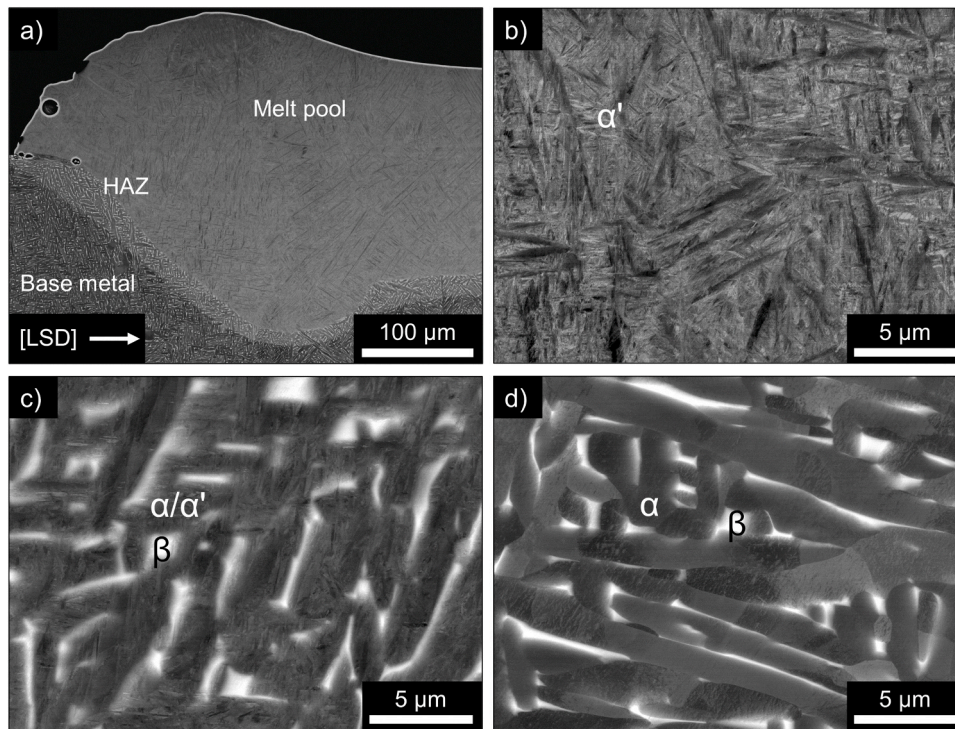


Figure 13. BSE images for $^{Ar}[Ti]_{75-106}^{Med}$ a) Beginning of the melt track displaying the melt pool, HAZ, and base metal b) Higher magnification image of the melt pool, c) HAZ d) Base metal. Note that the low magnification image in (a) of all three regions has been flipped such that the LSD is left to right.

coarsening of the prior- β grains. The prior- β texture of the melt pool region largely adopted the texture of the PBF-EB base. That being said, these inferences are made from the handful of large prior- β grains visible in the base metal portion of Fig. 14c.

The phase fraction map is shown in Fig. 14d, where the blue (darker) shaded region is indexed as α and the green (lighter) regions are β . Note that EBSD is unable to quantify the difference between α and α' , therefore only qualitative inferences can be made when discussing the phase fractions of these two phases. However, when discussing the β phase, this remains trivial as it is body-centered cubic compared to the hexagonal α and α' phases. The phase fraction of β across the three regions were calculated from the EBSD to be: 2.2% β – Melt pool, 6.9% β – HAZ, and 1.6% β – Base metal. This increase in β phase fraction is consistent with observations of the HAZ from the in situ laser melting of wrought Ti-6Al-4V and is likely due to the HAZ being over the β -transus temperature of the material ($\approx 1000^\circ\text{C}$) as was predicted in our previous work [22].

The HAZ thickness in $^{Ar}[Ti]_{75-106}^{Med}$ is similar in thickness to the HAZ from the previous in situ melting investigation of wrought Ti-6Al-4V [22], approximately $16\ \mu\text{m}$ to $20\ \mu\text{m}$, and is shown at equal magnification in Fig. 15. Fig. 15a displays the 3 regions (melt pool, HAZ, base metal) of wrought Ti-6Al-4V (Grade 5, NIST SRM 654b [23]) with a bimodal (equiaxed/lamellar) base metal microstructure. This image is of the *Scan-Key* condition in Ref. [22] (*Scan-Key* referring to keyhole mode melting during a laser scan. A SEM FOV is shown in this work), where the bare metal (no powder on top) was melted with the same laser and imaging setup at 201.3 W with a $120\ \mu\text{m}$ laser spot size at 700 mm/s scan speed. The HAZ in Fig. 15a consists of $\alpha/\alpha'/\beta$ phases, similar to the mixed phases in the HAZ observed in $^{Ar}[Ti]_{75-106}^{Med}$ (Fig. 13c). The morphology of the PBF-EB base Ti-6Al-4V in the present investigation (Fig. 15b) is α/β Widmanstätten, therefore the HAZ is going to closely resemble this morphology of the parent microstructure (Fig. 15b). However, the phase fractions of α/β are different, along with the acicular morphology which is likely α' . Pictorially, it appears that the melt pool α' in $^{Ar}[Ti]_{75-106}^{Med}$ (Fig. 15b) that grew from the HAZ seed crystals is

slightly more directional than that of the melt pool of the wrought Ti-6Al-4V (Fig. 15a). That is, some of the α' laths grew with more jagged spacing, mimicking the directions of the α/β parent HAZ. This could be due to the tighter spacing of the parent α/β Widmanstätten as opposed to the large equiaxed parent α/β in the wrought condition.

4. Conclusion

In situ melting and X-ray imaging experiments were conducted on Ti-6Al-4V alloy where the base material consisted of previously-built PBF-EB Ti-6Al-4V metal, and the same feedstock powder that was used to make this base as the powder to be melted during the in-situ experiments, in order to simulate the subsequent layer in a powder-bed fusion process. Below are the key takeaways from this work:

- Pores in the melt pool can result from residual gas pores that were already present in the starting powder that was generated during the powder atomization/manufacturing process. This precursor porosity (approximately 1%) was proportional to the size of the powder particle. These residual gas pores were observed to be released into the liquid during melting, and subsequently trapped in the solidified material.
- The layer of powder relative to the powder size plays a significant role in the generation of a uniform melt track/profile. That is, this powder layer height is different than the phrasing of *layer height* in traditional PBF-L techniques, where *layer height* pertains to the height of a melted layer relative to the previous layer. The results suggest that there may be deleterious effects in the powder melting if the PSD is changed for a given packed height if a system is optimized for a different PSD.
- When the thickness of the powder layer atop of the base is too great, the laser will not be able to melt into the base material and results in droplet formation above the surface.
- The pore-generating effects of the processing cover gas (Ar or He) were more closely related to the flow rate of said gasses as opposed to

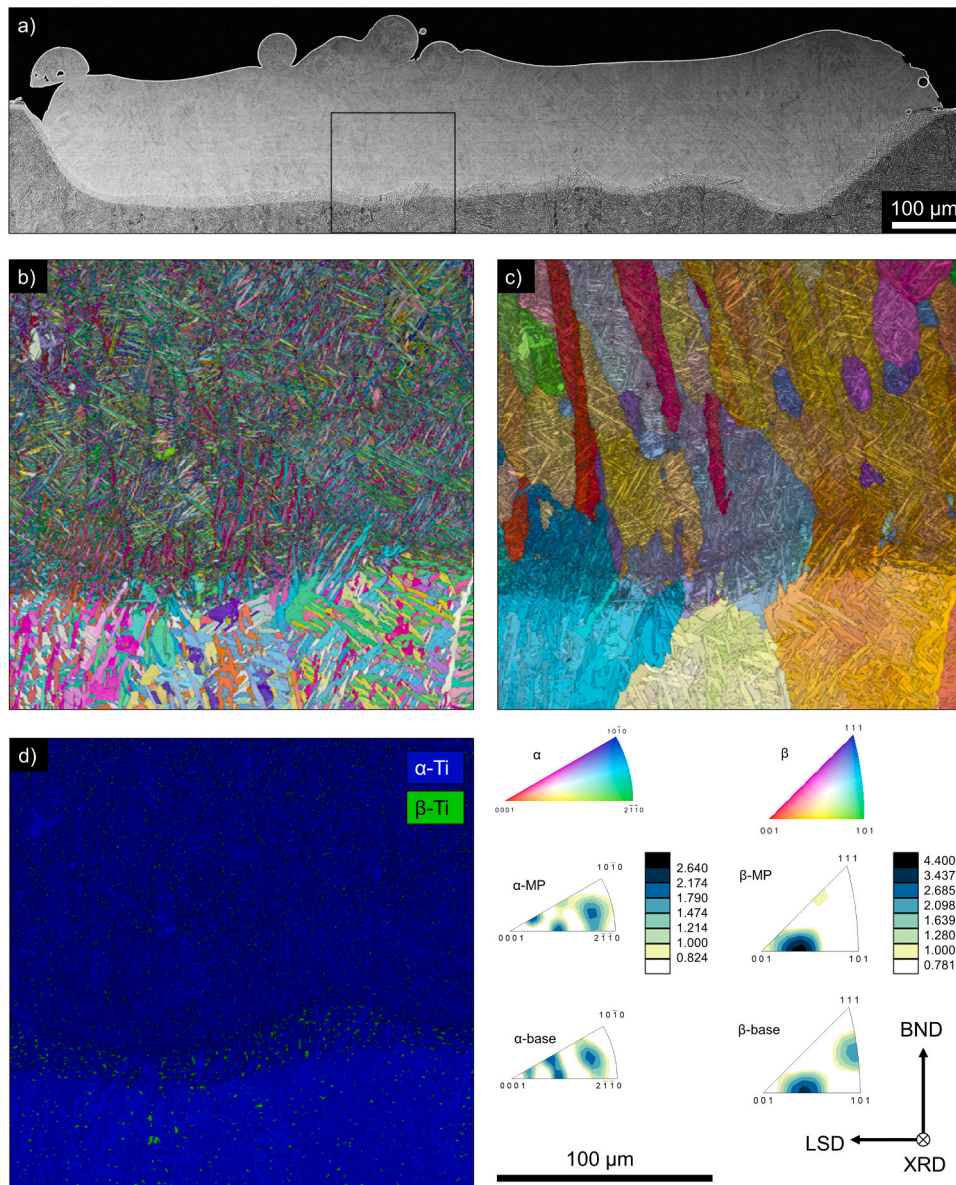


Figure 14. a) BSE image of the full FOV of the $Ar[Ti]_{75-106}^{Med}$ melt track with identifying rectangle for where the EBSD was collected, b) inverse pole figure map (oriented in the BND), c) Prior- β reconstruction, d) phase fraction map. Relevant IPF legend information for b)-c) is presented at the bottom right. MP = melt pool, base = base metal.

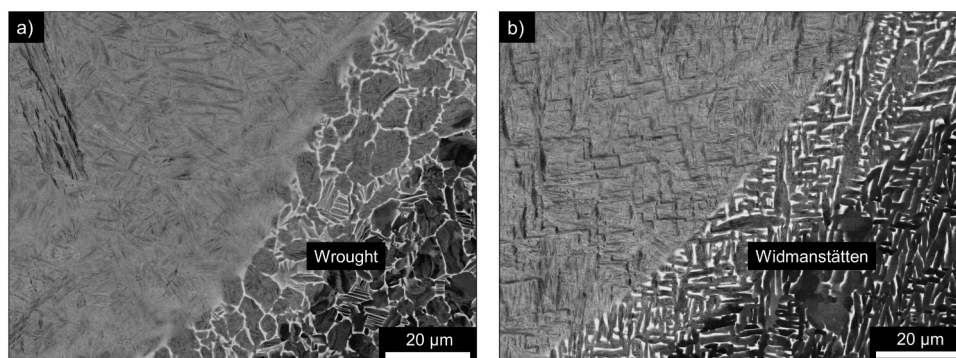


Figure 15. BSE images at equal magnification for a) Wrought laser melted Ti-6Al-4V from Ref. [22] b) $Ar[Ti]_{75-106}^{Med}$ (this work). Note, that the image in (a) has been flipped to match the LSD of (b).

the thermal properties of the gas for these particular experiments. This is not to say that the use of these two gasses had no thermal effect, but rather, the effects of the heat transfer differences of the two gasses were overshadowed by the difference in flow rates through the same flowmeter. The experiment with He cover gas had more gas pores, likely due to this increase in gas flow.

- The added tracer particles (W, Ta) allowed for observation of the counterclockwise motion away from the laser path, consistent with previous studies. When tracking the motion of the moving pores within the melt pool relative to the added tracer particles, the speed of the pores were considerably slower.
- The microstructure of the melt tracks show three distinct regions, all having similar crystallographic texture: the melt pool region (rapidly solidified) consisting of α' , the heat affected zone (HAZ) containing α' , α , and β phases as well as increased phase fraction of β relative to the base metal (consistent with the HAZ exceeding the β -transus temperature), and the base metal that remained unchanged by the experiments (α/β Widmanstätten microstructure). The melt pool texture adopted the texture from the base metal texture.
- The thickness of the HAZ in the PBF-EB base was similar in thickness to the wrought Ti-6Al-4V from previous work [22]. However, the α' phase present in the melt pool contained morphology more closely resembling the lath shapes/directions of the α/β Widmanstätten base microstructure and HAZ.

In light of these findings, the first hypothesis proposed, that particle size changes melt pool behavior is likely validated. However, the second hypothesis, that the change in thermal properties between cover gases would influence solidification dynamics could not be proven.

Future studies seek to systematically investigate the effects of different powder size distributions relative to powder layer height, as well as utilize new advancements at the 32-ID beamline at Argonne National Laboratory's Advanced Photon Source that can accommodate electron beam melting as opposed to laser melting [51].

CRedit authorship contribution statement

Nicholas Derimow: Writing – review & editing, Writing – original draft, Visualization, Validation, Resources, Methodology, Investigation, Formal analysis, Data curation, Conceptualization. **Nik Hrabe:** Writing – review & editing, Supervision, Project administration, Funding acquisition, Conceptualization. **Suveen Mathauhd:** Writing – review & editing, Supervision. **Kamel Fezzaa:** Supervision, Methodology. **Samuel J. Clark:** Writing – review & editing, Supervision, Resources, Methodology, Data curation. **Edward J. Garboczi:** Writing – review & editing, Visualization, Validation. **Jake T. Benzing:** Writing – review & editing, Visualization, Investigation. **Orion L. Kafka:** Writing – review & editing, Writing – original draft, Visualization, Validation, Software, Methodology, Investigation, Formal analysis, Data curation, Conceptualization. **Madelyn Madrigal-Camacho:** Writing – review & editing, Writing – original draft, Investigation, Formal analysis.

Declaration of Competing Interest

The authors declare that they have no known competing financial interests or personal relationships that could have appeared to influence the work reported in this paper.

Acknowledgments

The authors would like to acknowledge Skye Stuckey of 3D Systems for their contributions to the chemical analysis, Elisabeth Mansfield of NIST for supplementary SEM, Keenan Hanson of Stryker for providing materials for this research. This research used resources of the Advanced Photon Source, a U.S. Department of Energy (DOE) Office of Science

user facility operated for the DOE Office of Science by Argonne National Laboratory under Contract No. DE-AC02–06CH11357.

Appendix A. Supporting information

Supplementary data associated with this article can be found in the online version at [doi:10.1016/j.jalms.2024.100070](https://doi.org/10.1016/j.jalms.2024.100070).

References

- [1] W.S. Harun, N.S. Manam, M.S. Kamariah, S. Sharif, A.H. Zulkifly, I. Ahmad, H. Miura, A review of powdered additive manufacturing techniques for Ti-6Al-4V biomedical applications, *Powder Technol.* 331 (2018) 74–97, <https://doi.org/10.1016/j.powtec.2018.03.010>.
- [2] S. Chowdhury, N. Yadaiah, C. Prakash, S. Ramakrishna, S. Dixit, L.R. Gupta, D. Buddhi, Laser powder bed fusion: a state-of-the-art review of the technology, materials, properties & defects, and numerical modelling, *J. Mater. Res. Technol.* 20 (2022) 2109–2172, <https://doi.org/10.1016/j.jmrt.2022.07.121>.
- [3] D.-G. Ahn, Directed Energy Deposition (DED) process: state of the art, *Int. J. Precis. Eng. Manuf. -Green. Technol.* 8 (2) (2021) 703–742, <https://doi.org/10.1007/s40684-020-00302-7>.
- [4] N. Hrabe, T. Quinn, Effects of processing on microstructure and mechanical properties of a titanium alloy (Ti-6Al-4V) fabricated using electron beam melting (EBM), Part 2: energy input, orientation, and location, *Mater. Sci. Eng. A* 573 (2013) 271–277, <https://doi.org/10.1016/j.msea.2013.02.065>.
- [5] M.D. Valentine, V. Dhokia, J. Flynn, S.A. McNair, A.J. Lunt, Characterisation of residual stresses and oxides in titanium, nickel, and aluminium alloy additive manufacturing powders via synchrotron X-ray diffraction, *Mater. Today Commun.* 35 (2023) 105900, <https://doi.org/10.1016/j.mtcomm.2023.105900>.
- [6] N.D. Parab, C. Zhao, R. Cunningham, L.I. Escano, K. Fezzaa, W. Everhart, A. D. Rollett, L. Chen, T. Sun, Ultrafast X-ray imaging of laser–metal additive manufacturing processes, *J. Synchrotron Radiat.* 25 (5) (2018) 1467–1477, <https://doi.org/10.1107/S1600577518009554>.
- [7] C. Zhao, K. Fezzaa, R.W. Cunningham, H. Wen, F. De Carlo, L. Chen, A.D. Rollett, T. Sun, Real-time monitoring of laser powder bed fusion process using high-speed X-ray imaging and diffraction, *Sci. Rep.* 7 (1) (2017) 1–11, <https://doi.org/10.1038/s41598-017-03761-2>.
- [8] S. Hocine, S. Van Petegem, U. Frommherz, G. Tinti, N. Casati, D. Grolimund, H. Van Swygenhoven, A miniaturized selective laser melting device for operating X-ray diffraction studies, *Addit. Manuf.* 34 (2020) 101194, <https://doi.org/10.1016/j.addma.2020.101194>.
- [9] S. Hocine, H. Van Swygenhoven, S. Van Petegem, C.S.T. Chang, T. Maimaitiyili, G. Tinti, D. FerreiraSanchez, D. Grolimund, N. Casati, Operando X-ray diffraction during laser 3D printing, *Mater. Today* 34 (2020) 30–40, <https://doi.org/10.1016/j.mattod.2019.10.001>.
- [10] A. Bhatt, Y. Huang, C.L.A. Leung, G. Soundarapandian, S. Marussi, S. Shah, R. C. Atwood, M.E. Fitzpatrick, M.K. Tiwari, P.D. Lee, In situ characterisation of surface roughness and its amplification during multilayer single-track laser powder bed fusion additive manufacturing, *Addit. Manuf.* 77 (2023) 103809, <https://doi.org/10.1016/j.addma.2023.103809>.
- [11] N. An, T. Hu, C. Chen, J. Wang, Z. Ren, Application of synchrotron x-ray imaging and diffraction in additive manufacturing: a review, *Acta Metall. Sin. (Engl. Lett.)* (2021), <https://doi.org/10.1007/s40195-021-01326-x>.
- [12] C. Ioannidou, H.-H. König, N. Semjatov, U. Ackelid, P. Staron, C. Körner, P. Hedström, G. Lindwall, In-situ synchrotron X-ray analysis of metal additive manufacturing: current state, opportunities and challenges, *Mater. Des.* 219 (2022) 110790, <https://doi.org/10.1016/j.matdes.2022.110790>.
- [13] H.D. Nguyen, A. Pramanik, A. Basak, Y. Dong, C. Prakash, S. Debnath, S. Shankar, I. Jawahir, S. Dixit, D. Buddhi, A critical review on additive manufacturing of Ti-6Al-4V alloy: microstructure and mechanical properties, *J. Mater. Res. Technol.* 18 (2022) 4641–4661, <https://doi.org/10.1016/j.jmrt.2022.04.055>.
- [14] T.S. Tshphepe, S.O. Akinwamide, E. Olevsky, P.A. Olubambi, Additive manufacturing of titanium-based alloys- a review of methods, properties, challenges, and prospects, *Heliyon* 8 (3) (2022) e09041, <https://doi.org/10.1016/j.heliyon.2022.e09041>.
- [15] A.N. Aufa, M.Z. Hassan, Z. Ismail, Recent advances in Ti-6Al-4V additively manufactured by selective laser melting for biomedical implants: prospect development, *J. Alloy. Compd.* 896 (2022) 163072, <https://doi.org/10.1016/j.jallcom.2021.163072>.
- [16] R. Liu, Z. Wang, T. Sparks, F. Liou, J. Newkirk, *Aerospace Applications of Laser Additive Manufacturing*, Elsevier Ltd, 2016, <https://doi.org/10.1016/B978-0-08-100433-3.00013-0>.
- [17] X. Li, C. Zhao, T. Sun, W. Tan, Revealing transient powder-gas interaction in laser powder bed fusion process through multi-physics modeling and high-speed synchrotron x-ray imaging, *Addit. Manuf.* 35 (May) (2020) 101362, <https://doi.org/10.1016/j.addma.2020.101362>.
- [18] N.P. Calta, A.A. Martin, J.A. Hammons, M.H. Nielsen, T.T. Roehling, K. Fezzaa, M. J. Matthews, J.R. Jeffries, T.M. Willey, J.R. Lee, Pressure dependence of the laser-metal interaction under laser powder bed fusion conditions probed by in situ X-ray imaging, *Addit. Manuf.* 32 (October 2019) (2020), <https://doi.org/10.1016/j.addma.2020.101084>.

- [19] C. Zhao, N.D. Parab, X. Li, K. Fezzaa, W. Tan, A.D. Rollett, T. Sun, Critical instability at moving keyhole tip generates porosity in laser melting, *Science* 370 (6520) (2020) 1080–1086, <https://doi.org/10.1126/science.abd1587>.
- [20] Z. Gan, O.L. Kafka, N. Parab, C. Zhao, L. Fang, O. Heinonen, T. Sun, W.K. Liu, Universal scaling laws of keyhole stability and porosity in 3D printing of metals, *Nat. Commun.* 12 (1) (2021) 2379, <https://doi.org/10.1038/s41467-021-22704-0>.
- [21] B.J. Simonds, J. Tanner, A. Artusio-Glimpse, P.A. Williams, N. Parab, C. Zhao, T. Sun, The causal relationship between melt pool geometry and energy absorption measured in real time during laser-based manufacturing, *Appl. Mater. Today* 23 (101049) (2021), <https://doi.org/10.1016/j.apmt.2021.101049>.
- [22] N. Derimow, E.J. Schwalbach, J.T. Benzing, J.P. Killgore, A.B. Artusio-Glimpse, N. Hrabe, B.J. Simonds, Corrigendum to: “in situ absorption synchrotron measurements, predictive modeling, microstructural analysis, and scanning probe measurements of laser melted Ti-6Al-4V single tracks for additive manufacturing applications, *J. Alloy. Compd.* 919 (2022) 165890, <https://doi.org/10.1016/j.jallcom.2021.163494>.
- [23] NIST SRM 654b, Standard Reference Material (SRM) 654b, Titanium Alloy, 6Al-4V, National Institute of Standards and Technology (2013).
- [24] ASTM F2924-14, Standard Specification for Additive Manufacturing Titanium-6 Aluminum-4 Vanadium with Powder Bed Fusion, ASTM Standards (2014). 10.1520/F2924-14.
- [25] ASTM B214-22, Test Method for Sieve Analysis of Metal Powders, ASTM Standards (2022). 10.1520/B0214-22.
- [26] ASTM B822-17, Standard Test Method for Particle Size Distribution of Refractory Metal Powders and Related Compounds by Light Scattering, ASTM Standards (2017). 10.1520/B0822-17.
- [27] N. Derimow, E. Mansfield, J. Holm, N. Hrabe, Additive manufacturing titanium powder oxygen variation within a single powder bed due to differences in powder size and oxygen content, *Addit. Manuf. Lett.* 5 (2023) 100125, <https://doi.org/10.1016/j.addlet.2023.100125>.
- [28] E.J. Garboczi, N. Hrabe, Particle shape and size analysis for metal powders used for additive manufacturing: technique description and application to two gas-atomized and plasma-atomized Ti64 powders, *Addit. Manuf.* 31 (November 2019) (2020) 1–13, <https://doi.org/10.1016/j.addma.2019.100965>.
- [29] E.J. Garboczi, N. Hrabe, Three-dimensional particle shape analysis using x-ray computed tomography: experimental procedure and analysis algorithms for metal powders, *J. Vis. Exp.* 166 (2020) 61636, <https://doi.org/10.3791/61636>.
- [30] H. Ali, L. Ma, H. Ghadbeigi, K. Mumtaz, In-situ residual stress reduction, martensitic decomposition and mechanical properties enhancement through high temperature powder bed pre-heating of selective laser melted Ti6Al4V, *Mater. Sci. Eng.: A* 695 (2017) 211–220, <https://doi.org/10.1016/j.msea.2017.04.033>.
- [31] ASTM E1409-13, Standard Test Method for Determination of Oxygen and Nitrogen in Titanium and Titanium Alloys by Inert Gas Fusion, ASTM Standards (2013). 10.1520/E1409.
- [32] ASTM E1447-09, Standard Test Method for Determination of Hydrogen in Titanium and Titanium Alloys by Inert Gas Fusion Thermal Conductivity / Infrared Detection, ASTM Standards((Reapproved 2016)) (2009). 10.1520/E1447-09R16.
- [33] ASTM E1941-10, Standard Test Method for Determination of Carbon in Refractory and Reactive Metals, ASTM Standards (2016). 10.1520/E1941-10.
- [34] F. Cordelieres, *Manual Tracking* (2005).
- [35] J.-Y. Tinevez, N. Perry, J. Schindelin, G.M. Hoopes, G.D. Reynolds, E. Laplantine, S. Y. Bednarek, S.L. Shorte, K.W. Eliceiri, TrackMate: an open and extensible platform for single-particle tracking, *Methods* 115 (2017) 80–90, <https://doi.org/10.1016/j.ymeth.2016.09.016>.
- [36] J. Schindelin, I. Arganda-Carreras, E. Frise, V. Kaynig, M. Longair, T. Pietzsch, S. Preibisch, C. Rueden, S. Saalfeld, B. Schmid, J.-Y. Tinevez, D.J. White, V. Hartenstein, K. Eliceiri, P. Tomancak, A. Cardona, Fiji: an open-source platform for biological-image analysis, *Nat. Methods* 9 (7) (2012) 676–682, <https://doi.org/10.1038/nmeth.2019>.
- [37] C. Pautzon, S. Van Petegem, E. Hryha, C. SinTingChang, S. Hocine, H. Van Swygenhoven, C. De Formanoir, S. Dubiez-LeGoff, Effect of helium as process gas on laser powder bed fusion of Ti-6Al-4V studied with operando diffraction and radiography, *Eur. J. Mater.* 2 (1) (2022) 422–435, <https://doi.org/10.1080/26889277.2022.2081622>.
- [38] J.H. Lienhard IV, J.H. Lienhard, V. A Heat Transfer Textbook, Vol. Version 5.10, Phlogiston Press, 2020.
- [39] Q. Guo, M. Qu, L.I. Escano, S.M.H. Hojjatzadeh, Z. Young, K. Fezzaa, L. Chen, Revealing melt flow instabilities in laser powder bed fusion additive manufacturing of aluminum alloy via in-situ high-speed X-ray imaging, *Int. J. Mach. Tools Manuf.* 175 (2022) 103861, <https://doi.org/10.1016/j.ijmactools.2022.103861>.
- [40] S. Vock, B. Klöden, A. Kirchner, T. Weißgärber, B. Kieback, Powders for powder bed fusion: a review, *Prog. Addit. Manuf.* 4 (4) (2019) 383–397, <https://doi.org/10.1007/s40964-019-00078-6>.
- [41] R. Cunningham, Defect Formation Mechanisms in Powder-Bed Metal Additive Manufacturing, Ph.D. thesis, Carnegie Mellon University, Pittsburgh, PA (2018).
- [42] S.J. Wolff, H. Wang, B. Gould, N. Parab, Z. Wu, C. Zhao, A. Greco, T. Sun, In situ X-ray imaging of pore formation mechanisms and dynamics in laser powder-blown directed energy deposition additive manufacturing, *Int. J. Mach. Tools Manuf.* 166 (2021) 103743, <https://doi.org/10.1016/j.ijmactools.2021.103743>.
- [43] J. Yan, W. Yan, S. Lin, G. Wagner, A fully coupled finite element formulation for liquid–solid–gas thermo–fluid flow with melting and solidification, *Comput. Methods Appl. Mech. Eng.* 336 (2018) 444–470, <https://doi.org/10.1016/j.cma.2018.03.017>.
- [44] S. Tammas-Williams, H. Zhao, F. Léonard, F. Derguti, I. Todd, P. Prangnell, XCT analysis of the influence of melt strategies on defect population in Ti–6Al–4V components manufactured by selective electron beam melting, *Mater. Charact.* 102 (2015) 47–61, <https://doi.org/10.1016/j.matchar.2015.02.008>.
- [45] V. Prithivirajan, M.D. Sangid, The role of defects and critical pore size analysis in the fatigue response of additively manufactured IN718 via crystal plasticity, *Mater. Des.* 150 (2018) 139–153, <https://doi.org/10.1016/j.matdes.2018.04.022>.
- [46] J. Alegre, A. Díaz, R. García, L. Peral, I. Cuesta, Effect of HIP post-processing at 850°C/200 MPa in the fatigue behavior of Ti-6Al-4V alloy fabricated by selective laser melting, *Int. J. Fatigue* 163 (2022) 107097, <https://doi.org/10.1016/j.ijfatigue.2022.107097>.
- [47] C.J. Smithells, C.E. Ransley, The diffusion of gasses through metals, *Proc. R. Soc. A: Math., Phys. Eng. Sci.* 150 (869) (1935) 172–197, <https://doi.org/10.1098/rspa.1935.0095>.
- [48] S.-H. Li, J.-T. Li, W.-Z. Han, Radiation-induced helium bubbles in metals, *Materials* 12 (7) (2019) 1036, <https://doi.org/10.3390/ma12071036>.
- [49] J. Yang, H. Yu, J. Yin, M. Gao, Z. Wang, X. Zeng, Formation and control of martensite in Ti-6Al-4V alloy produced by selective laser melting, *Mater. Des.* 108 (2016) 308–318, <https://doi.org/10.1016/j.matdes.2016.06.117>.
- [50] A.I. Saville, S.C. Vogel, A. Creuziger, J.T. Benzing, A.L. Pilchak, P. Nandwana, J. Klemm-Toole, K.D. Clarke, S.L. Semiatin, A.J. Clarke, Texture evolution as a function of scan strategy and build height in electron beam melted Ti-6Al-4V, *Addit. Manuf.* 46 (June) (2021) 102118, <https://doi.org/10.1016/j.addma.2021.102118>.
- [51] L.I. Escano, S.J. Clark, A.C. Chuang, J. Yuan, Q. Guo, M. Qu, W. Dong, X. Zhang, J. Huang, K. Fezzaa, P. Kenesei, B.J. Walker, T. Sun, K.W. Eliceiri, L. Chen, An electron beam melting system for in-situ synchrotron X-ray monitoring, *Addit. Manuf. Lett.* 3 (2022) 100094, <https://doi.org/10.1016/j.addlet.2022.100094>.